# Xie. et al.

## Supplemental Material

**Restitution.** Restitution is the cell's response to a premature stimulus. If a stimulus is given at a long diastolic interval (Figure S1, upper), the following action potential duration (APD) will be normal. But if the stimulus is premature, the following APD will be shorter. The plot of the following APD as a function of the previous DI is the APD restitution curve (Fig S1, lower).

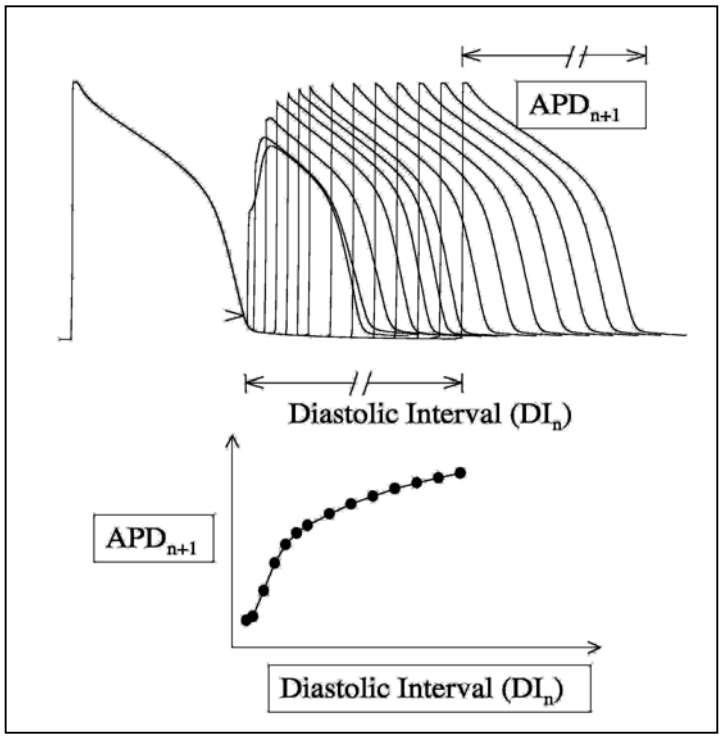


**Fig S1.** Definition of APD and DI (upper) and of the APD restitution curve (lower).

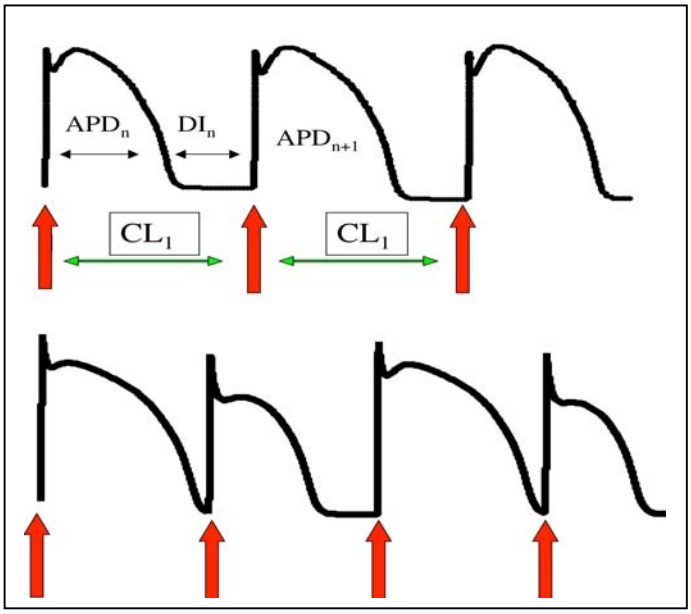


**Figure S2**. A cell that is periodically paced at a long cycle length will respond with a constant APD *(upper)*. But if the same cell is paced at a shorter cycle length, the response will be an *alternans,* an alternation of short and long APDs. *(lower)*

**Dynamics of Restitution.** Why is restitution dynamically important? Consider the cell paced at a constant rate $CL_1$ (Figure S2). In the upper tracing the cell is paced at a slower rate and produces a string of action potentials with a constant APD. But in the lower case, the faster pacing created shorter DIs, so restitution begins to have an effect. The short DI #1 following beat #1 leads to a shortened APD #2, but then that allows a longer diastolic interval DI #2, so APD #3 is again long, which leaves a shortened DI #3, so APD #4 is short. In this way, alternans can be generated by constant pacing and a sufficiently steep restitution curve.

This argument was first formulated by cardiologists Nolasco and Dahlen (2). For a given CL, the restitution relation, going from $DI_n$ to $APD_{n+1}$, can be coupled to the definition $APD_{n+1}$= CL-$DI_{n+1}$ to give a repetitive process, that is, a dynamics (Figure S3). This dynamics can converge or it can diverge. Whether the process coverges to a static equilibrium or diverges depends on the slope of the APD restitution curve. If its slope is >1 at the point at which it crosses the CL definition line, the equilibrium is unstable and the processs will diverge. Thus, a steeply sloped APD restitution curve will produce oscillations in APD, such as alternans (Figure S4).

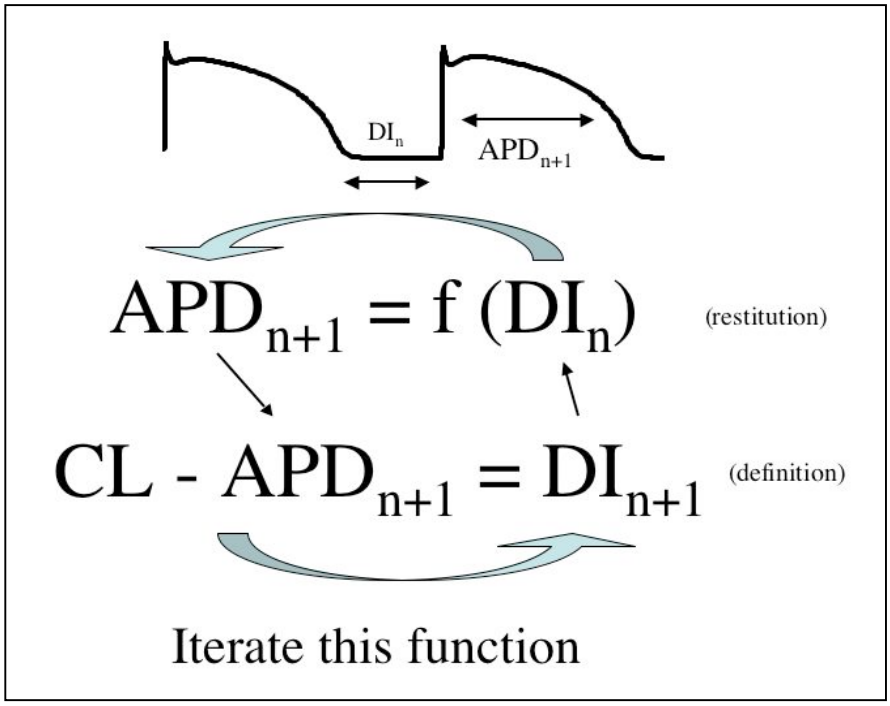


**Figure S3.** The APD restitution curve together with the definition of cycle length for constant pacing, together give a repeatable function, whose dynamics may be stable or unstable.

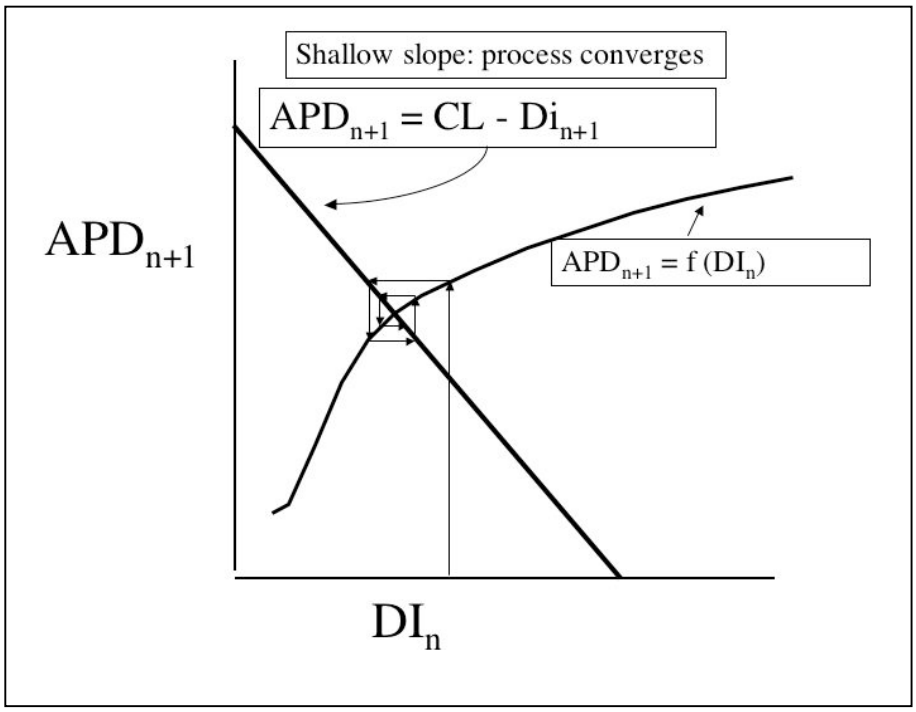


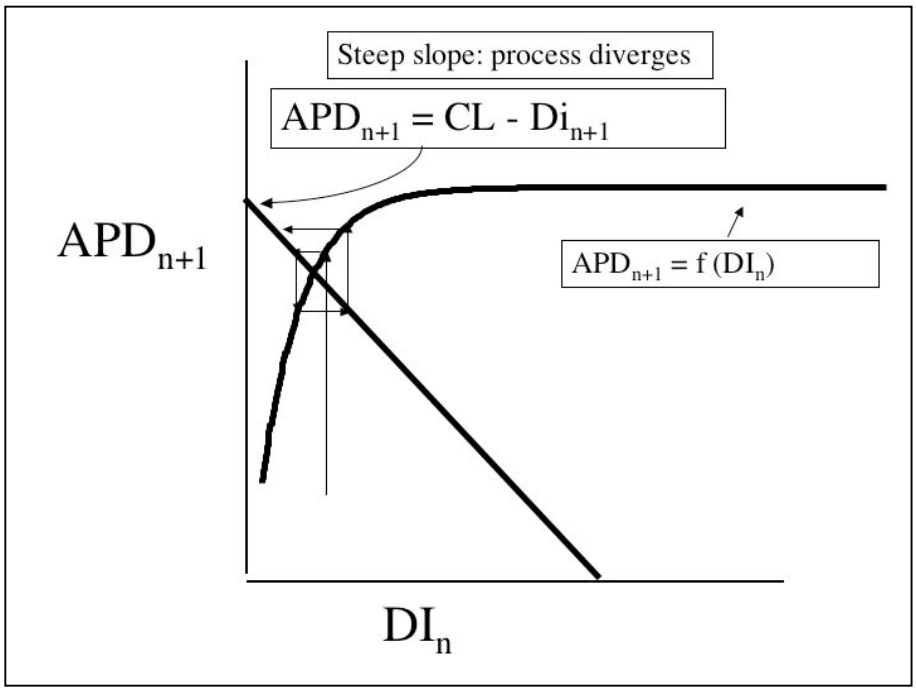


**Figure S4.** The process of going back and forth between the two functions is equivalent to the process (called "cobwebbing") of reflecting alternately between the two graphs, resulting in convergence (*upper*, shallow slope) or divergence (*lower*, steeper slope).

**Dynamics due to restitution can create wavebreak**. In the traditional view, wavebreak requires heterogeneities, represented by the black triangle in Fig. S5.

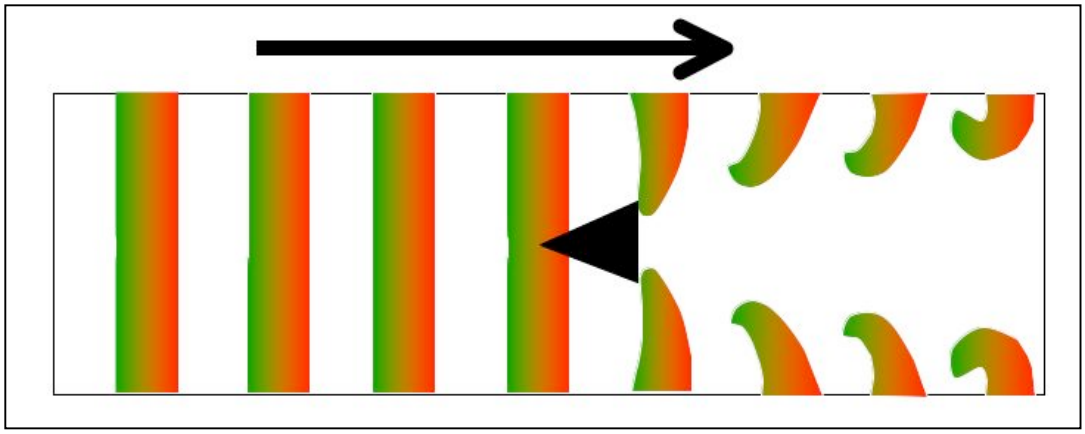

**Figure S5 (above).** Schematic representation of a tissue heterogeneity, such as an infarct or fibrotic region, causing wavebreak. The heterogeneity, represented by the black triangle, breaks the wave as it passes from left to right. **Figure S6 (below).** Illustration of dynamic wavebreak. See text for details.

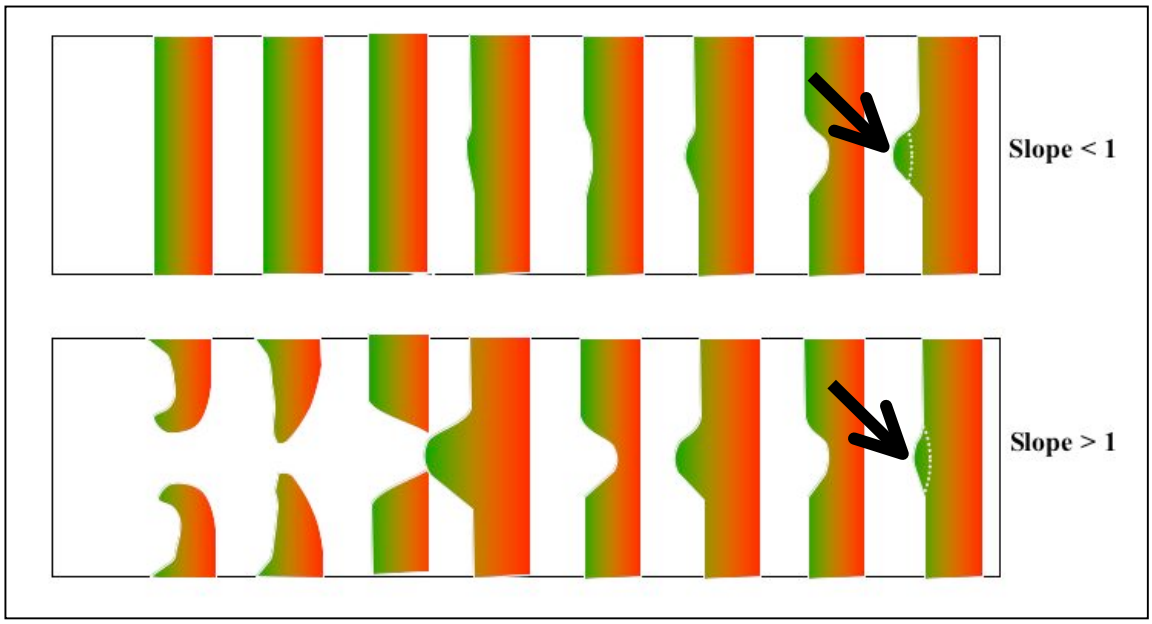


Wavebreak can also be generated dynamically. In the dynamic scenario (Figure S6), the upper panel shows the case in which the slope of the APD restitution curve was shallow, and the lower panel shows the steep case. In both cases, perturbations (marked by the arrows) were inserted into the wavebacks, that is, a prolongation of the local APD and subsequent reduction of the following DI (white area). The perturbation in the shallow case (top) was large, and the perturbation in the steep case (bottom) was smaller. *Note that the steeply-sloped restitution causes the small perturbation to grow, whereas the shallowly-sloped curve causes the large perturbation to vanish. The growing perturbation in the steeply-sloped case eventually causes wavebreak.*

# Methods

## Cell Model

In the original LR1 model, the maximum conductances of the ionic currents were: $G_{Na} = 23 mS/cm^2$, $G_{si} = 0.09 mS/cm^2$ and $G_K = 0.282 mS/cm^2$. With these values, the LR1 model has an APD of ~360ms. We modified the parameters from the original LR1 model as follows. First, we fixed $G_{Na} = 16 mS/cm^2$, in keeping with recent literature (3). Second, we set $G_K = 0.423 mS/cm^2$, in order to bring the APD to a more realistic value of around 200 ms. Third, we sped up $Ca^{2+}$ kinetics by a factor of 2, i.e., $\tau_d \rightarrow 0.5\tau_d$, and $\tau_f \rightarrow 0.5\tau_f$, in keeping with more recent work (4).

## Anatomical Model

The data sets, of anatomy and fiber orientation for canine ventricle (5) were obtained courtesy of the Cardiac Mechanics Research Group at the University of California, San Diego. The geometry of the canine ventricles, in a Cartesian grid, is embedded in a 359 x 275 x 253 rectangular box. The real-world spacing between grid points is 0.025 cm.

In homogeneous tissue, the diffusion tensor can be simplified to $\tilde{D} = D_h \tilde{I}$, where $D_h = 0.001 cm^2/ms$, and $\tilde{I}$ is the 3x3 unit matrix. But real cardiac conduction is anisotropic, with a fast direction along the cardiac fiber and slower conduction in the transverse plane, while the fiber orientation itself varies systematically across the myocardium (5). The rotation of the preferred direction of conduction as one goes through the myocardium is called “fiber rotation” or “fiber twist”. In the model with

fiber rotation, cardiac tissue anisotropy is determined by the diffusion tensor $\tilde{D}(x,y,z)$. We implemented the method of (6) to generate this 3x3 diffusion tensor $\tilde{D}$ from the vectors of fiber orientation.

At each point in the 3D anatomy of the ventricles, the cardiac microstructure has three principal directions: one along the myocardial fiber $\dot{f}_{//}$, the second, orthogonal to the fiber direction and lying in the myocardial sheet plane $\dot{f}_{\perp}^{1}$, and the third, orthogonal to the above two vectors, in the cross-sheet direction $\dot{f}_{\perp}^{2}$. In the local or fiber coordinate system constructed by the three orthogonal vectors, the diffusion tensor is diagonal

$$D = \begin{pmatrix} D_{//} & 0 & 0 \\ 0 & D_{\perp} & 0 \\ 0 & 0 & D_{\perp} \end{pmatrix}$$

Here $D_{//} = 0.001 cm^2/ms$ is the diffusion constant along the fiber direction, and $D_{\perp} = 0.00025 cm^2/ms$ is the transverse diffusion constant. The three vectors $\dot{f}_{//}$, $\dot{f}_{\perp}^{1}$ and $\dot{f}_{\perp}^{2}$ are the corresponding eigenvectors of the diffusion tensor $\tilde{D}$ with eigenvalues $D_{//}$, $D_{\perp}$ and $D_{\perp}$, respectively. Using standard matrix transformations, we obtained the diffusion tensor $\tilde{D}$ as

$$\tilde{D} = ADA^T$$

where $A=(\dot{f}_{//}, \dot{f}_{\perp}^{1}, \dot{f}_{\perp}^{2})$ is the orthogonal transform between the tensors D and $\tilde{D}$, and $A^T$ is its transpose matrix. Using the fact that $AA^T = \tilde{I}$, the diffusion tensor $\tilde{D}$ has the following form

$$\tilde{D} = D_{\perp}\tilde{I} + (D_{//} - D_{\perp})\dot{f}_{//}\dot{f}_{//}^{T}, \qquad (4)$$

where $\tilde{I}$ is the unit matrix, $\dot{f}_{//}$ is the normalized vector of fiber orientation, and $\dot{f}_{//}^{T}$ is its

transpose vector. So the diffusion tensor $\widetilde{D}$ depends only on the fiber vector $\dot{f}_{//}$, whose value at each point in the canine ventricles was obtained from the original anatomical data.

The distribution of fiber angles at a representative level of the heart (Figure S7), is mostly continuous, with occasional discontinuities at the boundaries between the septum and the free wall. This compares well with actual data (Figure S8).

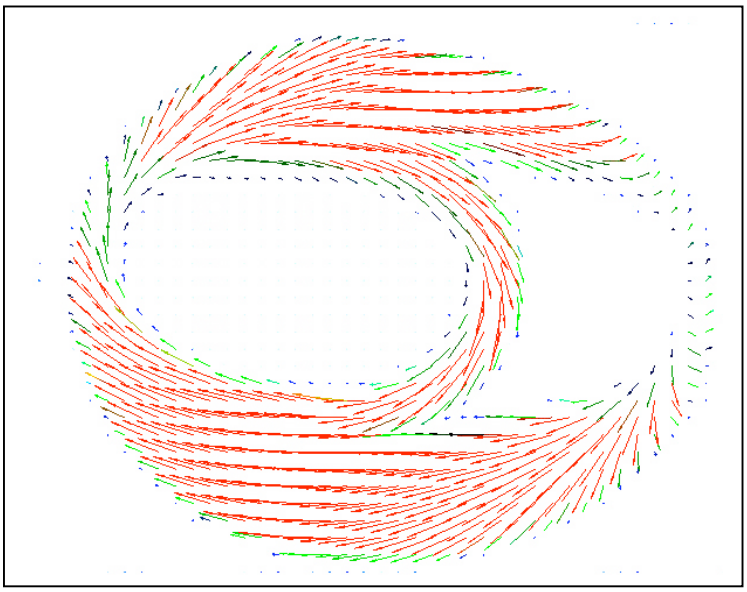

**Figure S7.** Fiber angles at a representative section perpendicular to the long axis of our heart model. Color denotes angle with the plane of section: red fibers are in the plane, and blue fibers perpendicular to it, with intermediate colors in between.

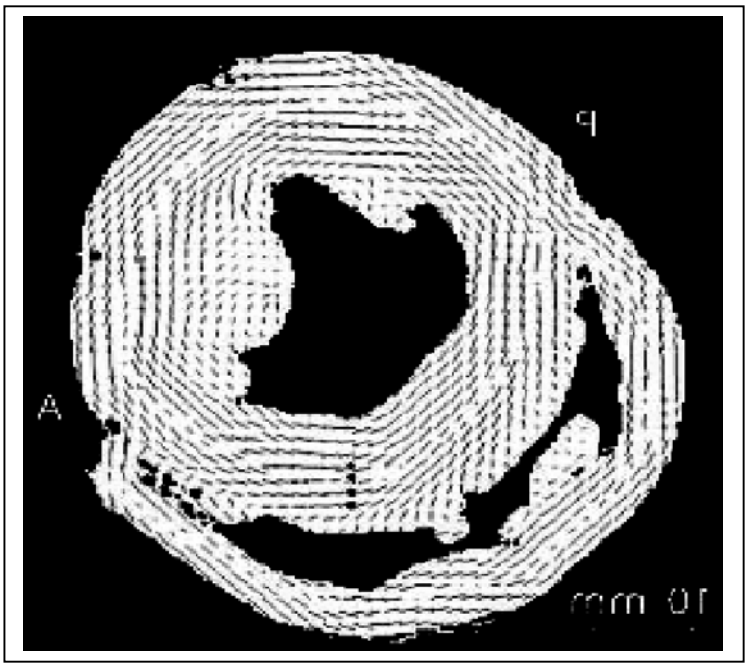


**Figure S8.** Fiber angles at a comparable plane of goat heart, as determined by diffusion tensor MRI imaging. (Geerts, L., Bovendeerd, P., Nicolay, K., and Arts, T. 2002. Characterization of the normal cardiac myofiber field in goat measured with MR-diffusion tensor imaging. *Am J Physiol Heart Circ Physiol* 283:H139-145).

**Numerical Methods.**

The conventional Euler method for integrating our equations is computationally tedious and costly for a detailed cellular model and complex anatomical model. Therefore, we solved the Partial Differential Equation using the well-known operator splitting method. We split the nonlinear operator ($I_{ion}$ term) and the diffusion operator in Eq. (1) in the paper into two terms, and then integrated the two terms separately and alternatively. We used a forward Euler method to integrate the diffusion term, and a time adaptive second-order Runge-Kutta method ($\Delta t_{\min} \le 0.01 ms$ and $\Delta t_{\max} \le 0.1 ms$) to integrate the ordinary differential equation of the reaction term, with its gating variable equations and the equation describing intracellular calcium concentration. The time step of integration of the PDE was set to $\Delta t_{\max}$ to keep all cells synchronized. The numerical methods and criteria for assuring numerical stability have been provided previously in detail (7). We checked for convergence by repeatedly shortening space and time steps, and saw only the small quantitative changes reported in that paper.

Numerical simulations for 2D homogeneous tissue were run on DEC Alpha workstations with a single processor, while simulations for 3D cardiac tissue required a multi-processor supercomputer and parallelized code. The traditional parallel method usually places the irregular structure or object into a 3D box, and then simply divides the 3D box along one direction by the required processors. The main drawback of this method is that each processor then has a different number of heart cells to compute, which strongly depends on the shape of the object. Speed is limited by the processor with

the largest number of cells, since all other processors with fewer cells to compute must wait for its synchronization before the next step, detracting significantly from performance. The second disadvantage is that this method requires a great deal of memory, much of which is allocated to unused spaces which are not "in" the heart. When the canine ventricles are placed in the minimal bounding box (359 x 275 x 253), grid points that are "in" the heart are only 1/3 of the total. To overcome these two drawbacks, we first mapped the irregular geometry of the canine ventricles onto a one-dimensional sequenced array, rather than a large 3D cube, with several additional arrays to record each cell's neighbors. Then we divided the one-dimensional array uniformly over the number of processors, with each processor having the same load, such that memory was allocated only for real cells. Combination of this parallel method (implemented in the MPI language) and the adaptive time step operator-splitting method (7) permitted reasonable-time simulations of electrical wave activities, even in the whole heart. One second of simulation of the canine ventricle model took about two hours, using 30 processors, each rated at 1.4 GHz.

The space step was set $dx=dy=dz=0.025cm$ for all 2D and 3D simulations. Our 2D homogeneous tissue consisted of 400 x 400 nodes, corresponding in physical dimensions to a 10 x 10 $cm^2$ square, with no-flux boundary conditions at the edges. For the 3D anatomy simulations, we implemented the boundary conditions as follows. Each point $C(i,j,k)$ in the ventricles has six nearest neighbors $N(i\pm1,j,k)$, $N(i,j\pm1,k)$, $N(i,j,k\pm1)$, which were used to calculate the diagonal diffusion terms, and twelve next-nearest neighbors $N(i\pm1,j\pm1,k)$, $N(i\pm1,j,k\pm1)$, $N(i,j\pm1,k\pm1)$, to calculate the cross-diffusion terms (The indices $i$, $j$ and $k$ represent the x, y and z-axis directions,

respectively). For the grid points whose nearest neighbors do not all belong to the heart, we created virtual cells by the following rule: if $N(i \pm 1, j, k)$ was not on the heart, then it was identical to $N(i \mp 1, j, k)$ if $N(i-1, j, k)$ or $N(i+1, j, k)$ was in the heart; otherwise both $N(i+1, j, k)$ and $N(i-1, j, k)$ were identical to the cell $C(i, j, k)$. The same rule applied to the indices *j* and *k*. For grid points whose next-nearest neighbors did not all belong to the heart, in addition the above rule for the diagonal term, we created virtual cells for the cross-diffusion terms: if $N(i \pm 1, j \pm 1, k)$ did not belong to the heart, then it was identical to $N(i \pm 1, j \mp 1, k)$ if $N(i \pm 1, j-1, k)$ or $N(i \pm 1, j+1, k)$ was in the heart, otherwise both $N(i \pm 1, j-1, k)$ and $N(i \pm 1, j+1, k)$ were identical to $C(i, j, k)$. The same rules applied for the indices (i,k) and (j,k). This implementation produced smooth wave propagation and electrical wave speed in good agreement with observations.

**Electrophysiological measurements**

APD restitution refers to the relationship between APD and the previous diastolic interval (DI). APD was defined as the duration during which $V > -72mV$, and DI as the portion during which $V < -72mV$. APD restitution was measured in a one-dimensional ring, and obtained by progressively shortening the length of the ring until conduction failed.

Scroll waves were initiated by using two successive planar waves, the first initiated at the apex and propagating upward to the base, and the second initiated in the LV perpendicular to the first. The tip of a spiral wave in a 2D sheet (or in a plane intersecting the ventricle in 3D) was defined as the intersection point of two successive -30 mV contour lines, measured 2 ms apart. The filament of a 3D scroll wave is defined as

the set of tips of the corresponding stack of 2D waves, one for each plane intersecting the ventricle. We recorded the trajectories inscribed on the epicardium by these filaments

A virtual electrocardiogram (ECG) was calculated:

$$ECG = \iiint \sum_{i=1}^{3} \sum_{j=1}^{3} \tilde{D}_{i,j} (\nabla V)_j (\nabla (1/R))_i \, dxdydz,$$

where $R$ is the distance from a lead to the location of the dipole (6).

## Results

### Statistics of VF

We recorded the statistical properties of wavelets during simulated VF.

**TABLE 1**

| | Gsi=0 | Gsi=0.025 | Gsi=0.045 | Gsi=0.060 |
|---|---|---|---|---|
| 2D homogeneous tissue | 44.3 | 60.0 | 105.6 | 140.5 |
| 3D homogeneous model of canine ventricles | 44.7 | 60.4 | 104.9 | 86.2 |
| 3D model of canine ventricles with fiber rotation | 45.5 | 60.5 | 75.7 | 88.9 |

Table 1. Average cycle lengths (ms) of reentry for the various models.

**TABLE 2**

| Filaments | LV | RV | Sep | Base | Apex |
|---|---|---|---|---|---|
| 600 – 1600 (ms) | 23±15 ***(.35± .23)*** | 9±5 ***(.38± .21)*** | 8±5 ***(.43± .23)*** | 22±12 ***(.32± .18)*** | 18±11 ***(.49± .29)*** |
| 1000 – 1600 (ms) | 33±8 ***(.51± .12)*** | 12±3 ***(.7± .13)*** | 10±3 ***(.54± .17)*** | 30±7 ***(.44± .10)*** | 25±5 ***(.68± .14)*** |

Table 2. Filament Numbers (upper entries) in the various regions of the ventricular model during VF. Below them are the corresponding densities (in parentheses) in filaments/mm$^3$. Note that the densities do not differ widely from one region to another.

## TABLE 3

| Whole Ventricle | Nonreentrant wavebreak lifespan (ms) | Reentry Episodes per Sec | Median Cycles per Reentry | Median cycle lengths (ms) | Reentrant wavebreak incidence |
|---|---|---|---|---|---|
| Epicardium | 38.9±22.5 ***(20±26)*** | 48 ***(40)*** | 1.8 (1-5) ***(2 (1-13))*** | 88.1±15.5 ***(83.1±13.6)*** | 97/570 (17.0%) ***(93/1203 (7.7%))*** |
| Endocardium | 35.1±18.0 ***(23±22)*** | 39 ***(79)*** | 1.6 (1-5) ***(3 (1-27))*** | 86.5±16.3 ***(80.8±1.4)*** | 78/402 (19.4%) ***(182/1392 (13.1%))*** |

Table 3. Statistics of reentry in RV during scroll wave breakup in simulated whole ventricle. Below the observed values, are the comparable values (in parentheses) seen in pig heart experimentally (8).

## Electrophysiological gradients.

As a preliminary study, we created a simple model of the electrophysiological differences among epicardial, endocardial and M-cells. We began with the LR1 model, then divided $I_K$ into $I_{Kr}$ and $I_{Ks}$. (3). We also added $I_{to}$, based essentially on Courtemanche's model (9), which is also very similar to the model of (10).

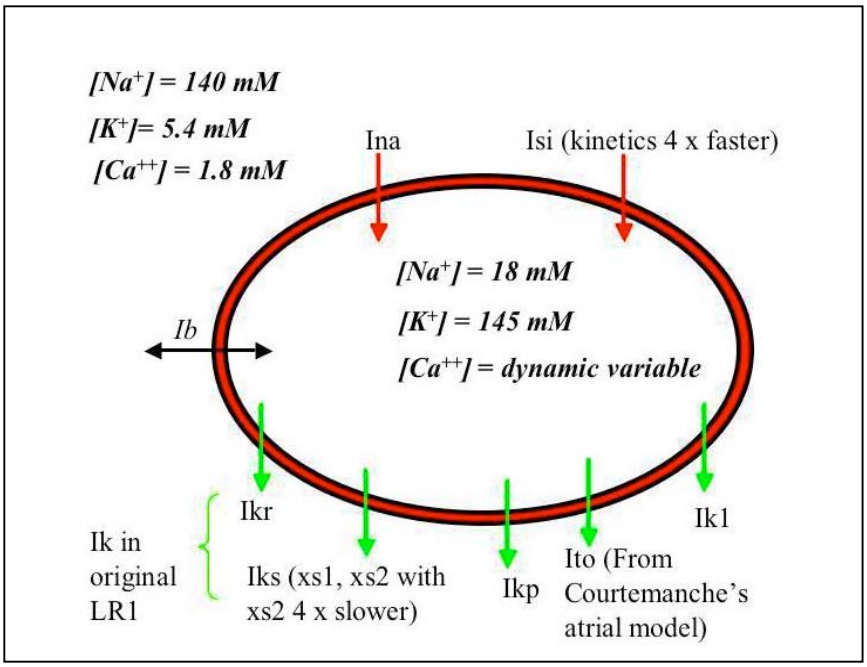


**Figure S9**. Schematic for constructing gradients in cell electrophysiological properties.

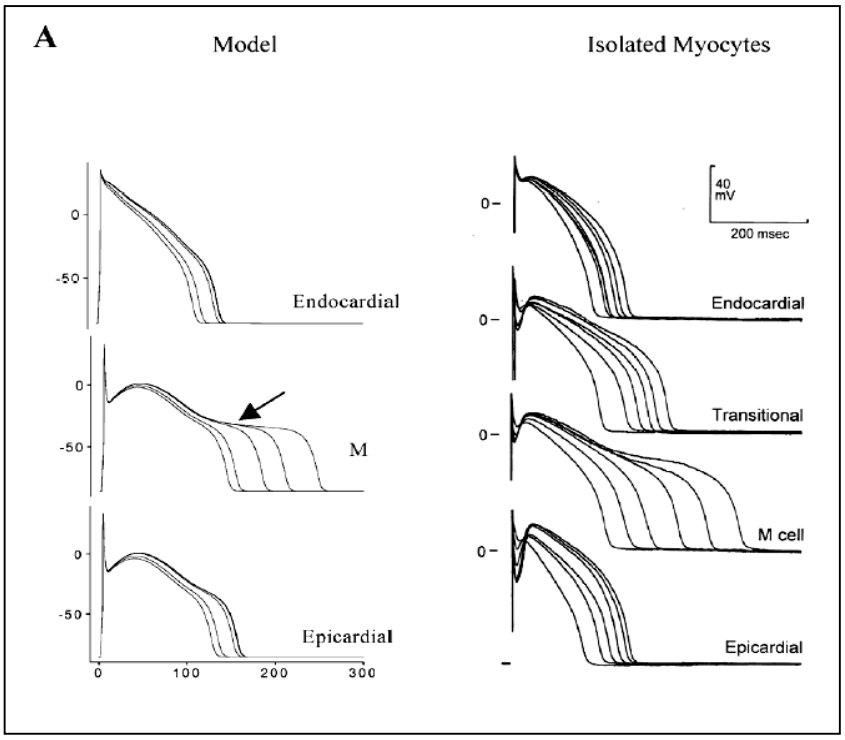


**Figure S10.** Simulations of our models of the three types of cells, *(left)* compared to actual cardiac myocytes (1) *(right)*

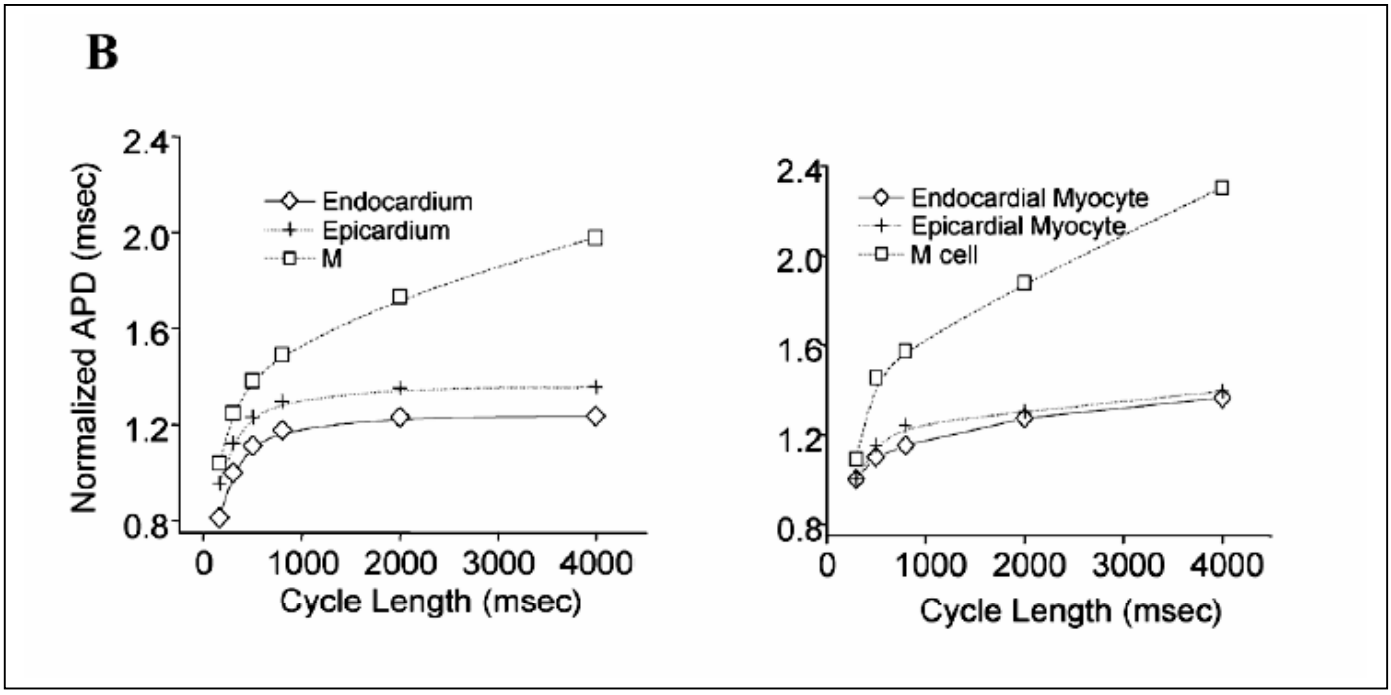


**Figure S11.** APD restitution curves for the 3 types of cell model (left) compared to actual restitution curves from cardiac myocytes (1).

Using these models in a 3D rectangular slab, we found that some scroll waves that did not break up in a homogeneous slab (with fiber anisotropy) *did* break up when placed in a heterogeneous tissue model with epi-, endo- and M-cells. (Movies 8 and 9). Thus, our principal finding was that the steeper restitution curves of M-cells did indeed play a destabilizing role, but we stress that this finding is preliminary, and more work needs to be done making a cell model that will exactly reproduce the experimental findings.

**Septal Initiation.**

We tested the hypothesis that the site of initiation of the reentrant wave could affect its tendency to breakup into fibrillation. As a preliminary study, we initiated reentrant waves inside the interventricular septum. (The other studies reported in this paper initiated reentry in the left ventricle.)

We found, in our limited experiments, that the site of initiation did not seem to significantly affect the fate of the scroll wave. If the dynamics were set to the stable meander regime ($G_{si} = 0.03$), a single scroll wave initiated in the septum continued to rotate intact. (Figure S12). But if the dynamics were set to the strong meander regime ($G_{si} = 0.045$), breakup occurred within about 1 second (Figure S13).

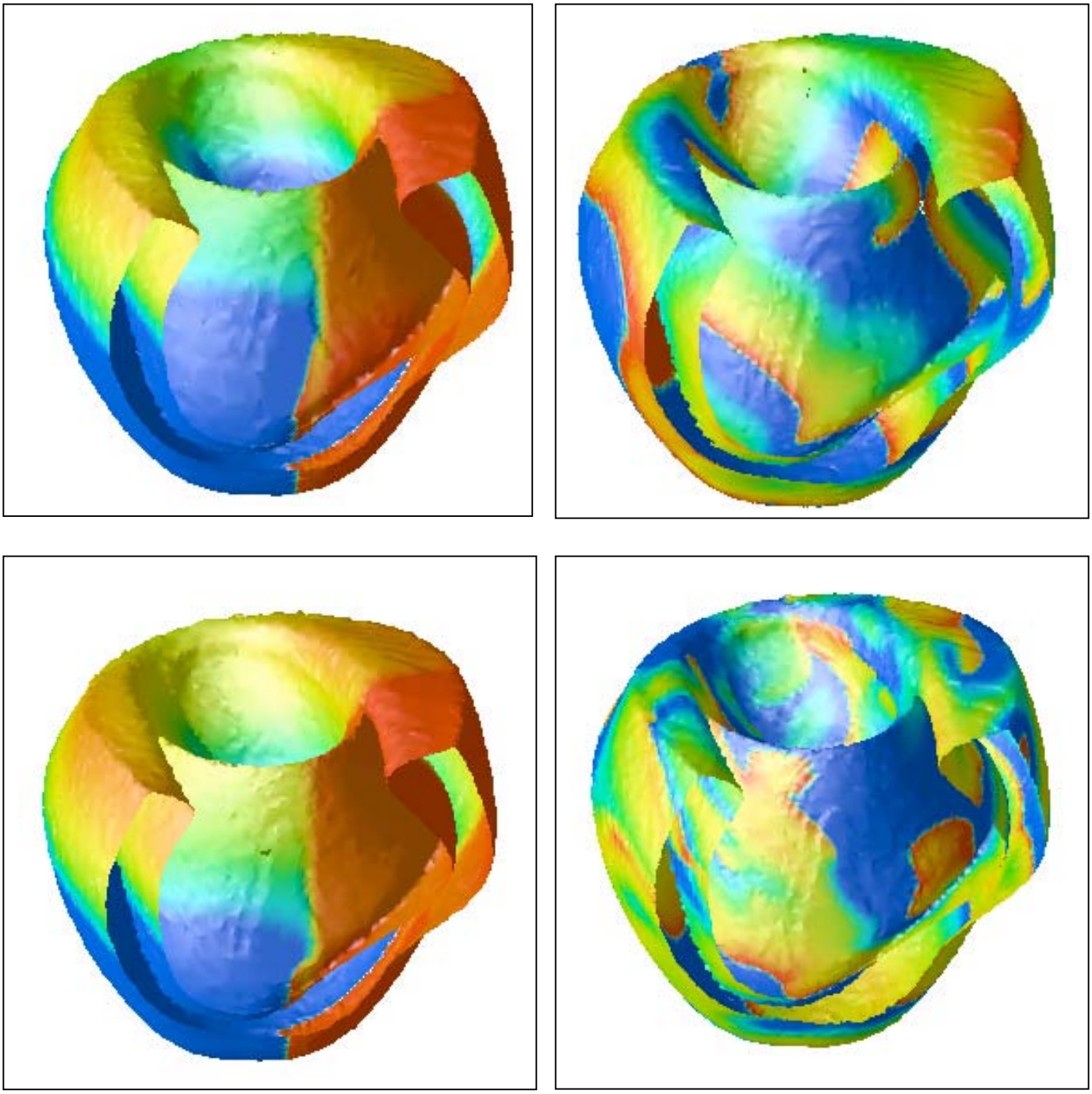

**Figure S12 (top).** A scroll wave initiated in the septum remains intact for $G_{si} = 0.30$.
**Figure S13 (bottom).** The same protocol for $G_{si} = 0.045$ results in breakup one second later.

## Movies

**Movie 1 (Hom_ssw.avi)**. Scroll wave dynamical behavior in canine ventricle model without fiber orientation. The grid size of the canine ventricular anatomy is 359 x 275 x 253, corresponding to a physical size of 8.975 x 6.875 x 6.325 $cm^3$. Each cell was modeled by the Luo-Rudy Phase I ventricular cell model. The maximum conductance of the slow inward calcium current, $G_{si}$=0. *Left*: Voltage on the surface (red=depolarized; blue=repolarized). *Middle*: Filaments of scroll wave reentry and tip trajectories of the filament on the epicardium. *Right*: Isosurfaces of voltage (V=-30 mV) in the canine ventricles. A scroll wave was initiated using two successive perpendicular planar waves, the first at the apex propagating upward to the base, and the second perpendicular to the first in the LV. The scroll wave remained intact and nearly stable after the initiated transient; its filament was straight, and the motion of the filament tip on the epicardium traced a circular pattern, confirming that the scroll wave was stable. The epoch shown here is 1400 ms.

**Movie 2 (Hom_msw.avi)**. Scroll wave dynamical behavior in canine ventricle model without fiber orientation for $G_{si}$=0.025. The scroll wave also remained intact, and the straight filament tip traced a meandering flower pattern. The epoch is 1380 ms.

**Movie 3 (Hom_hsw.avi)**. Scroll wave dynamical behavior in canine ventricle model without fiber orientation for $G_{si}$=0.045. Although the scroll wave remained intact, the

initiated straight filament became twisted, and the waves displayed large irregular spatial oscillations. The epoch is 1800 ms.

**Movie 4 (Hom_breakup.avi)**. Dynamics of scroll wave breakup in canine ventricle model without fiber orientation for $G_{si}$=0.060. The initiated scroll wave broke up, after several rotations, into complex multiple wavelets, producing a fibrillation-like state. The epoch is 2260 ms.

**Movie 5 (fiber_ssw.avi)**. Scroll wave dynamical behavior in canine ventricle model with fiber orientation for $G_{si}$=0. The initiated scroll wave remained intact, but its filament became folded and twisted, due to the fiber rotation, and its wave tip on the epicardium traced a meandering, rather than circular path. The epoch is 1460 ms.

**Movie 6 (fiber_msw.avi)**. Scroll wave dynamical behavior in canine ventricle model with fiber orientation for $G_{si}$=0.025. The initiated scroll wave filament folded enough to cause the wavefront to break through the epicardium, but the twisted filament remained itself intact, and the scroll wave tip on the epicardium meandered widely. The epoch is 1440 ms.

**Movie 7 (fiber_breakup.avi)**. Scroll wave breakup in canine ventricle model with fiber orientation for $G_{si}$=0.045. The initiated scroll wave quickly broke up into unstable multiple wavelets, after nearly one second or ~7 rotations. The continual generation and annihilation of waves maintained the complex VF-like state. The epoch is 1360 ms.

**Movie 8 (3types.avi).** Scroll wave breakup takes place here in a 3D rectangular slab with fiber anisotropy, into which we have introduced three types of cell model, representing epi- endo- and M-cells. Tissue thickness is 15 mm, and the three layers are equal in thickness.

**Movie 9 (3types_split.avi).** The same simulation as Movie 8 is shown in three separated layers, so the initial breakup occurring in the M-cell layer is clear.

## References (Supplement)


1. Liu, D.W., and Antzelevitch, C. 1995. Characteristics of the delayed rectifier current (IKr and IKs) in canine ventricular epicardial, midmyocardial, and endocardial myocytes. A weaker IKs contributes to the longer action potential of the M cell. *Circ Res* 76:351-365.
2. Nolasco, J.B., and Dahlen, R.W. 1968. A graphic method for the study of alternation in cardiac action potentials. *J.Appl.Physiol.* 25:191-196.
3. Luo, C.H., and Rudy, Y. 1994. A dynamical model of the cardiac ventriclar action potential: II. Afterdepolarization, triggered activity, and potentiation. *Circ. Res.* 74:1097-1113.
4. Xu, A.X., and Guevara, M.R. 1998. Two forms of spiral-wave reentry in an ionic model of ischemic ventricular myocardium. *Chaos* 8:157-174.
5. Nielsen, P.M.F., Grice, I.J.L., Smaill, B.H., and Hunter, P.J. 1991. Mathematical model of geometry and fibrous structure of the heart. *Am. J. Physiol.* 260:H1365-H1378.
6. Panfilov, A. 1997. Modeling of re-entrant patterns in an anatomical model of the heart. In *Computational Biolgy of the Heart*. A.P.a.A. Holden, editor. NY: Wiley. 259-276.
7. Qu, Z., and Garfinkel, A. 1999. An advanced algorithm for solving partial differential equation in cardiac conduction. *IEEE Trans Biomed Eng* 46:1166-1168.

8. Valderrabano, M., Yang, J., Omichi, C., Kil, J., Lamp, S.T., Qu, Z., Lin, S.F., Karagueuzian, H.S., Garfinkel, A., Chen, P.S., et al. 2002. Frequency analysis of ventricular fibrillation in swine ventricles. *Circ Res* 90:213-222.
9. Courtemanche, M., Ramirez, R.J., and Nattel, S. 1998. Ionic mechanisms underlying human atrial action potential properties: insights from a mathematical model. *Am J Physiol* 275:H301-321.
10. Priebe, L., and Beuckelmann, D.J. 1998. Simulation study of cellular electric properties in heart failure. *Circ Res* 82:1206-1223.